Total and orbital density-based analyses of molecules revealing long-range interaction regions

Hasebe, Masatoshi
Tsutsumi, Takuro
Taketsugu, Tetsuya
Tsuneda, Takao

(Citation)
Journal of Computational Chemistry,44(31):2391-2403

(Issue Date)
2023-12-05

(Resource Type)
journal article

(Version)
Accepted Manuscript

Total and orbital density-based analyses of molecules revealing long-range interaction regions

Masatoshi Hasebe[*], Takuro Tsutsumi[†], Tetsuya Taketsugu[‡], Takao Tsuneda[§]

July 2, 2023

Abstract

Total and orbital electron densities of molecules are explored for the effect of the long-range correction (LC) for density functional theory (DFT) exchange functionals by comparing to the effect of the *ab initio* coupled cluster singles and doubles (CCSD) method. Calculating the LC effect on the total electron densities shows that the LC stabilises the electrons around the long-range interaction regions of kinetic energy density, which are assumed to be electrons other than free electrons and self-interacting electrons, while the CCSD method stabilises the electrons in the long-range interaction regions in the vertical molecular planes. As a more precise test, the LC effect on orbital densities are compared to the CCSD effect on Dyson orbital densities. Surprisingly, these effects are similar for the unoccupied orbitals, indicating that the LC covers the effects required to reproduce the CCSD Dyson unoccupied orbitals. For exploring the discrepancies between these effects on the occupied orbitals, the photoionisation cross sections are calculated as a direct test for the shapes of the HOMOs to investigate the differences between these effects on the occupied orbitals. Consequently, the LC clearly produces the canonical HOMOs close to the CCSD Dyson and experimental ones, except for the HOMO of benzene molecule that mixes with the HOMO−1 for the CCSD Dyson orbitals. This indicates that the orbital analyses using the photoionisation cross sections are available as a direct test for the quality of DFT functionals.

Keywords: Density Functional Theory, Long-range correction, Total density analysis, Orbital density analysis, Quality test of functionals ■

[*]Graduate School of Chemical Sciences and Engineering, Hokkaido University, Sapporo 060-0810, Japan 1

[†]Department of Chemistry, Faculty of Science, Hokkaido University, Sapporo 060-0810, Japan 2, L-Station, Creative Research Institution (CRI), Hokkaido University, Sapporo 060-0812, Japan 3

[‡]Department of Chemistry, Faculty of Science, Hokkaido University, Sapporo 060-0810, Japan 2, Institute for Chemical Reaction Design and Discovery (WPI-ICReDD), Hokkaido University, Sapporo 001-0021, Japan 4

[§]Department of Chemistry, Faculty of Science, Hokkaido University, Sapporo 060-0810, Japan 2, Graduate School of System Informatics, Kobe University, Nada-ku, Kobe, Hyogo 657-8501, Japan 5, Corresponding author. e-mail: takaotsuneda@sci.hokudai.ac.jp

1 Introduction

In density functional theory (DFT), long-range correction (LC)[1] for the exchange functionals is installed in major quantum chemistry calculation programs as long-range corrected (range-separated) functionals, such as LC-X (X is a usual functional),[2] CAM-B3LYP,[3] LC-ωPBE,[4] ωB97,[5] and tuned range-separation[6] functionals, improved the calculated chemical properties such as charge transfer excitation energies[7] and high-order optical response properties.[8,9] The quantitative orbital energies of LC-DFT,[12,13] which are given for both the occupied and unoccupied orbitals for the first time ever, are accepted as the main reason for dramatically improving chemical properties. The reactive orbital energy theory,[14] which discusses reactions based on orbital energy variations, is developed as an electronic theory for reactions using quantitative orbital energies. This theory reproduces the electronic theory diagrams of organic chemistry[15] and reveals the one-to-one correspondence between the orbitals of the most varied orbital energies and the intrinsic reaction coordinates (IRCs) of the reaction processes.[16] Regardless of these achievements, it is unclear how the LC modifies DFT functionals to provide the electronic states of molecules accurately.

Electron density is gaining popularity as a property for evaluating the quality of DFT functionals.[17–19] Consider that the v-representability of electron density,[20] which is the fundamental concept of DFT that establishes the correspondence between density and potential, implies that the quality of total electron density is equivalent to that of the corresponding potential. Some studies have compared the calculated total electron densities for many DFT functionals to those of the *ab initio* coupled-cluster singles and doubles (CCSD) method,[21] which are calculated using the coupled-perturbed method.[22] Therefore, it is shown that the gaps between calculated electron densities significantly increase for recently developed functionals, such as semi-empirical functionals with many parameters. The electron density difference from the CCSD result can be a good index for evaluating the quality of the functionals. Actually, the applicability of DFT functionals has often been investigated from the viewpoint of electron density by comparing to the CCSD and higher-order results.[10,11] The local density-based quality test of DFT functionals, however, has been controversial, mainly due to the questionable assumption that the best DFT functional should reproduce the local electron density of the CCSD wavefunction. Chemical properties, which are usually response properties, depend on orbitals not on total density.[23] One-electron density is preferred over total density, even for v-representability, because the Hohenberg-Kohn theorem[20] establishes the mapping to one-electron external (nuclear-electron) potential v, which acts on orbital density.

The Dyson orbital, which is interpreted as the molecular orbital of *ab initio* many-electron wavefunction methods,[24] is a useful tool for analysing electronic states based on orbital density. The Dyson orbital is the one-electron wavefunction of the all-electron wavefunction, which is calculated using the neutral- and ionised-state wavefunctions (for the details, see Sec. 2.3). The occupied and unoccupied orbital energies are defined as the minus signs of ionisation potentials and electron affinities for the Dyson orbitals, respectively. The experimental values are well reproduced when the Dyson orbitals are used to calculate photoionisation cross-sections in photoelectron spectra,[25] indicating the high accuracy of the Dyson orbitals. Therefore, the quality of DFT functionals can be evaluated by comparing the canonical orbital densities of DFT functionals to the corresponding Dyson orbital densities. This also

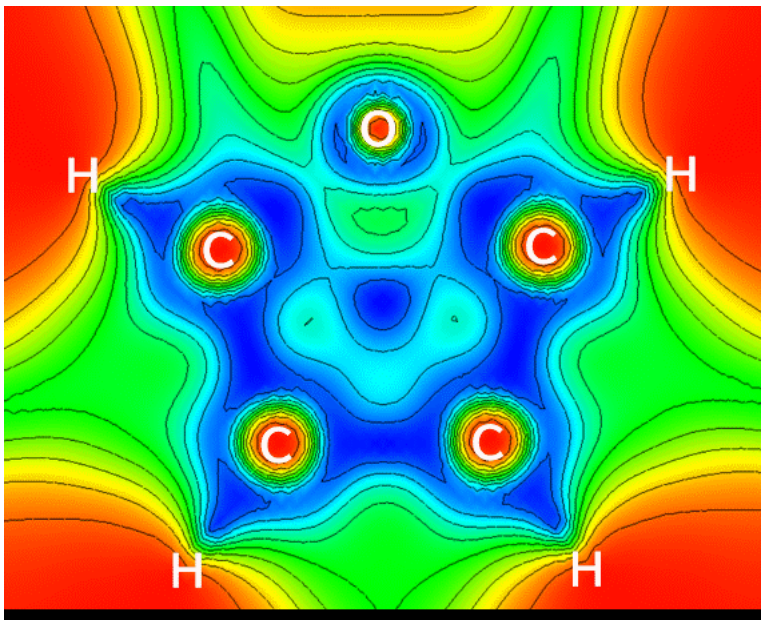

Figure 1: Contour plot of the ratio of the von Weizsäcker kinetic energy density to the total one, t_σ ($0 \leq t_\sigma \leq 1$) in Eq. (3), for the electronic state of the furan molecule. The colour levels are drawn to have ten equal parts. In the plot, the reddish regions, where t_σ is close to one, indicate the self-interaction regions, while the blueish regions, where t_σ is close to zero, show the free-electron regions. The remaining green regions are called long-range interaction regions.

indicates that the effect of the LC on the orbitals can be discussed in terms of orbital density.

In this context, a method for analysing the electronic states of molecules based on the von Weizsäcker kinetic energy density is available[26] (for details, see Sec. 2.1). Plotting the of the von Weizsäcker kinetic energy density to the total one shows that two types of the electronic state regions appear in molecules: one is a free-electron region for t_σ close to zero and another is a self-interaction region for t_σ close to one, represented by blue and red regions in Fig. 1, respectively. It should be noted that there are middle regions in green where there are neither near σ bonds in the free electron regions nor atomic cores in the self-interaction regions. They are known as long-range interaction regions, because the LC has small effects on either σ bonds or atomic cores. However, as far as we know, it has yet to be confirmed that the LC affects the electrons in the long-range interaction regions.

In this study, we investigate the LC effects on the total electron and orbital densities of molecules by comparing them to the effects of the CCSD method, and then discuss the availability of this analysis for evaluating the quality of DFT functionals.

2 Related theories

2.1 Kinetic energy density-based analysis and transversal physical relation

There is a method for visually classifying the electronic states of molecule that uses the von Weizsäcker kinetic energy density,[27]

$$\tau^{\mathrm{W}} = \sum_{\sigma} \tau_{\sigma}^{\mathrm{W}} = \sum_{\sigma} \frac{1}{8} \frac{|\boldsymbol{\nabla}\rho_{\sigma}|^2}{\rho_{\sigma}}, \tag{1}$$

where ρ_σ is σ-spin electron density. This method uses the relation for self-interacting electrons, which interact only with the opposite-spin electrons in the same orbitals. Therefore, the exact kinetic energy density, τ, becomes the von Weizsäcker one, τ^{W}, in Eq. (1),[28]

$$\tau = \sum_{\sigma} \tau_{\sigma} = -\frac{1}{2} \sum_{\sigma} \boldsymbol{\nabla}^2 P_{\sigma}(\mathbf{r}_1, \mathbf{r}_2) \Big|_{\mathbf{r}_1 = \mathbf{r}_2} \rightarrow \tau^{\mathrm{W}}. \tag{2}$$

Since the von Weizsäcker kinetic energy density is positive definite, plotting the ratio of the von Weizsäcker kinetic energy density τ_σ^{W} to the total one τ_σ,

$$t_{\sigma} = \frac{\tau_{\sigma}^{\mathrm{W}}}{\tau_{\sigma}} \quad (0 \leq t_{\sigma} \leq 1), \tag{3}$$

where σ is the spin of electrons, reveals two regions of electronic states in molecules: i.e., the free-electron region, where electrons behave like the free electrons of transition metals, and the self-interaction region, where electrons behave like those in hydrogen atomic orbital that interact only with the opposite-spin electrons in the same orbitals. The electron localisation function is developed using this relationship to identify localised electronic groups[29] and successfully determine chemical bonds and electron pairs.[30–32]

Interestingly, different physical relations are established for the free-electron and self-interaction regions.[26] In the free-electron regions, there is a transversal physical relation between kinetic, exchange and correlation energies[26] through the parameter-free (PF) exchange,[33]

$$E_{\mathrm{x}} \equiv -\frac{1}{2} \sum_{\sigma} \int \rho_{\sigma}^{4/3} K_{\sigma} d^3\mathbf{r}, \tag{4}$$

$$K_{\sigma}^{\mathrm{PF}} = \frac{27\pi}{10\tau_{\sigma}} \rho_{\sigma}^{5/3} \left(1 + \frac{7x_{\sigma}^2 \rho_{\sigma}^{5/3}}{216\tau_{\sigma}}\right), \tag{5}$$

where $x_\sigma = |\boldsymbol{\nabla}\rho_\sigma|/\rho_\sigma^{4/3}$, and one-parameter progressive (OP) correlation[34] functionals,

$$E_c^{\mathrm{OP}} = -\int d^3\mathbf{r} \rho_{\alpha}\rho_{\beta} \frac{1.5214\beta_{\alpha\beta} + 0.5764}{\beta_{\alpha\beta}^4 + 1.1284\beta_{\alpha\beta}^3 + 0.3183\beta_{\alpha\beta}^2}, \tag{6}$$

$$\beta_{\alpha\beta} = q_{\alpha\beta} \left(\rho_{\alpha}^{-1/3} K_{\alpha}^{-1} + \rho_{\beta}^{-1/3} K_{\beta}^{-1}\right)^{-1}, \tag{7}$$

where the values in Eq. (6), i.e., 1.5214, 0.5763, 1.1284, and 0.3183, are not semiempirical parameters but fundamental constants. In Eqs. (5) and (7), kinetic energy term τ_σ and exchange energy term K_σ are included in the PF exchange and OP correlation functionals, respectively. Consider that these kinetic and exchange energy terms satisfy the fundamental conditions of kinetic and exchange energies.[35] Moreover, it is proven that the PF exchange and OP correlation functionals obey the fundamental conditions of exchange and correlation energies for slowly-varying density. Since the electron densities of the free-electron regions are particularly slowly-varying, there is a transversal physical relation between kinetic, exchange and correlation energies in the free-electron regions.

In the self-interaction regions, there is also a relation derived from the density matrix for self-interacting electrons,[36]

$$P_\sigma = \rho_\sigma^{1/2}(\mathbf{r}_1)\rho_\sigma^{1/2}(\mathbf{r}_2), \tag{8}$$

where ρ_σ is the density of σ-spin electrons and $\mathbf{r}_i$ is the position vector of the i-th electron. The exchange energy density $\epsilon_{\mathrm{x}\sigma}$ meets the far-from-nucleus (long-range) asymptotic behavior condition[37] based on this density matrix,

$$\epsilon_{\mathrm{x}\sigma}(\mathbf{r}) = -\frac{1}{2}\int d^3\mathbf{r}' \frac{|P_\sigma(\mathbf{r},\mathbf{r}')|^2}{|\mathbf{r}-\mathbf{r}'|} \xrightarrow{r\to\infty} -\frac{\rho_\sigma(\mathbf{r})}{2r}. \tag{9}$$

Furthermore, the parallel-spin correlation energy density is considered to be zero for self-interacting electrons, because the pair density matrix (the diagonal term of the second-order density matrix) becomes zero for parallel-spin electrons.

$$P_{2\sigma\sigma}(\mathbf{r}_1,\mathbf{r}_2) = \frac{1}{2}\left[\rho_\sigma(\mathbf{r}_1)\rho_\sigma(\mathbf{r}_2) - |P_\sigma(\mathbf{r}_1,\mathbf{r}_2)|^2\right] = 0. \tag{10}$$

In the self-interaction regions, the electron-electron interaction includes only the electron correlation between the opposite-spin electrons in the same orbital.

This study focuses on the green regions in Fig. 1, which are included in neither free-electron nor self-interaction regions and are found perpendicular to the σ bonds in the molecular planes. These green regions are referred to as "long-range interaction regions"[36] because the LC modifies exchange functionals that give accurate exchange energies for free-electron regions and hardly affects core orbital energies.[13] However, as far as we know, the LC has never been tested to see if it acts on electrons in this long-range interaction region.

2.2 Pseudospectral regional self-interaction correction

The regional self-interaction correction (RSIC)[38] is a self-interaction correction[39] using the kinetic energy density-based region-separation, which replaces the exchange energy density with the corresponding exchange self-interaction energy density only for the regions where t_σ is close to 1 (e.g., $t_\sigma \geq 0.97$). The pseudospectral (PS) RSIC[13] employs the PS exchange energy density[40] for the exchange self-interaction energy density as,

$$\epsilon_{\mathrm{x}}^{\mathrm{RSIC}} = \left[1 - f_{\mathrm{RS}}(t_\sigma)\right]\epsilon_{\mathrm{x}}^{\mathrm{DF}} + f_{\mathrm{RS}}(t_\sigma)\epsilon_{\mathrm{x}}^{\mathrm{SI}}, \tag{11}$$

$$\epsilon_{\mathrm{x}}^{\mathrm{SI}} = -\frac{1}{4}\sum_{\mu\nu\lambda\kappa}\int d^3\mathbf{r} P_{\mu\nu}P_{\lambda\kappa}\chi_\nu^*(\mathbf{r})\chi_\lambda(\mathbf{r})\int d^3\mathbf{r}'\frac{\chi_\kappa^*(\mathbf{r}')\chi_\mu(\mathbf{r}')}{|\mathbf{r}'-\mathbf{r}|}, \tag{12}$$

where $\epsilon_{\mathrm{x}}^{\mathrm{DF}}$ is a conventional exchange functional, f_{RS} is a region-separation function for clipping the self-interaction regions, $\mathbf{r}$ and $\mathbf{r}'$ are the position vectors of electrons, $P_{\mu\nu}$ is the $\mu\nu$-component of a density matrix, and χ_λ is the λ-th atomic orbital. This correction dramatically improves the calculated core excitation energies of long-range corrected functionals in time-dependent DFT calculations while maintaining the accuracy in the core ionisation energies, and valence, Rydberg, and charge transfer excitation energies.[41] Furthermore, this correction provides accurate orbital energies for core and valence orbitals simultaneously.[13] The significance of exchange self-interactions in the electronic states of molecules can be visualised by investigating the effect of PSRSIC on electron density.

2.3 Dyson orbitals and photoionisation cross sections

The Dyson orbital is a useful tool for calculating the orbital density of *ab initio* many-electron wavefunction methods.[24] The occupied and unoccupied Dyson orbitals are calculated using the neutral- and ionised-state wavefunctions as the one-electron wavefunction of a many-electron wavefunction such as,

$$\phi_{\mathrm{occ}}^{\mathrm{Dyson}}(\mathbf{r}_1) = \sqrt{N}\int d\mathbf{r}_2 \cdots d\mathbf{r}_N \Psi_{\mathrm{cat}}^*(\mathbf{r}_2, \cdots, \mathbf{r}_N)\Psi_{\mathrm{neu}}(\mathbf{r}_1, \mathbf{r}_2, \cdots, \mathbf{r}_N), \tag{13}$$

$$\phi_{\mathrm{unocc}}^{\mathrm{Dyson}}(\mathbf{r}_1) = \sqrt{N+1}\int d\mathbf{r}_2 \cdots d\mathbf{r}_{N+1} \Psi_{\mathrm{neu}}^*(\mathbf{r}_2, \cdots, \mathbf{r}_{N+1})\Psi_{\mathrm{ani}}(\mathbf{r}_1, \mathbf{r}_2, \cdots, \mathbf{r}_{N+1}), \tag{14}$$

where N is the total number of electrons in the neutral system, and Ψ_{neu}, Ψ_{cat} and Ψ_{ani} are the wavefunctions of neutral, cation and anion, respectively. Note that the Dyson orbitals of DFT wavefunctions correspond to the canonical orbitals, because DFT is a one-electron theory. The corresponding occupied and unoccupied orbital energies of the Dyson orbitals are defined as the minus signs of ionisation potentials and electron affinities, respectively.

For the Dyson orbitals, it has been reported thatthe calculated photoionisation cross-sections accurately reproduce the experimental photoelectron spectra.[25] The photoionisation cross sections σ_k are calculated as[42]

$$\sigma_k = \frac{4\pi^2 k E_{\mathrm{ir}}}{c}\left|D_k^{\mathrm{IF}}\right|^2, \tag{15}$$

where k is the magnitude of the photoelectron wavevector, E_{ir} is the energy of ionising radiation, and c is the speed of light. In Eq. (15), D_k^{IF} is the photoelectron dipole matrix element,

$$D_k^{\mathrm{IF}} = \mathbf{u}\left\langle \phi_{\mathrm{outermost}} \left|\mathbf{r}\right| \Psi_k^{\mathrm{el}} \right\rangle, \tag{16}$$

where $\mathbf{u}$ is the unit vector in the direction of the polarization of light, $\mathbf{r}$ is the dipole moment operator, $\phi_{\mathrm{outermost}}$ is the outermost one-electron wavefunction, which is HOMO in general, and Ψ_k^{el} is the photoelectron wavefunction,

$$\Psi_k^{\mathrm{el}} = \frac{1}{(2\pi)^{3/2}} e^{i\mathbf{k}\cdot\mathbf{r}}, \tag{17}$$

which is expressed as a sum of spherical partial waves.[42] By comparing the photoionisation cross-sections of the Dyson orbitals to those of the canonical orbitals of DFT functionals, the quality of these functionals can be discussed from the perspective of orbital density.

3 Computational details

Total electron density is calculated using the Kohn-Sham[36,43] orbitals, which are obtained by the LC[1,2] for the Becke 1988 (B88) exchange[44] + Lee-Yang-Parr correlation[45] (BLYP) functional (LC-BLYP) of the parameter μ=0.33 and the CCSD method[21] with the aug-cc-pVTZ basis set[46] except for benzene and cc-pVTZ for benzene. To explore the self-interaction regions, the PSRSIC[41] is also applied to the LC-BLYP. The kinetic energy density calculations are performed using the Multiwfn program.[47] Furthermore, the electron density differences are calculated using the output cube files containing the electron densities, which are calculated for the optimum geometries of LC-BLYP. The structures, orbitals and electron densities are illustrated using the ChemCraft program, while the contour plots are drawn using the VESTA program.[48] For the IRCs, the predictor-corrector integrator method[49,50] is used. The above calculations are performed with the Gaussian 16 Revision A.03 program,[51] while the PSRSIC calculations are performed with the development version of the GAMESS-US program.[52]

For orbital density calculations, the Kohn-Sham calculations are performed using the LC for the B88 exchange + one-parameter progressive correlation[34] (BOP) functional (LC-BOP) using the parameter μ=0.47, with the aforementioned basis set. As highly accurate orbitals, the Dyson orbitals in Eqs. (13) and (14) are also calculated for the CCSD wavefunction. The HF and BOP calculations are also performed for the photoionisation cross sections with the same basis set. For the Dyson orbital of the CCSD wavefunctions, the calculations are carried out using the equation-of-motion (EOM)-CCSD calculations in the Q-Chem program version 6.0.[53] The photoionisation cross section calculations are performed by setting the core charges of formaldehyde, water, benzene and cyclopentene as 0.25, 1.0, 0.15, and 0, considering the Franck-Condon factor only for formaldehyde, in the ezDyson program.[54] For the ionisation potentials that are not provided in the references, the experimental values given in the NIST Chemistry WebBook, SRD69[55] are used.

4 Results and Discussion

4.1 Long-range interaction regions in electron density

For revealing the long-range interaction from the viewpoint of electron density, the effects of the LC on the electron density is first compared to the von Weizsäcker kinetic energy density ratio t_σ in Eq. (3) in the molecular planes and vertical planes of formaldehyde and benzene molecules (Fig. 2). Figure 2 shows that the long-range interaction regions of t_σ, the greenish regions shown in the dotted lines of the left plots, overlap well with those of the LC, the reddish regions shown in the dotted lines of the second left plots. In both these plots, the long-range interaction regions of t_σ are found around the perpendicular directions from the σ bonds and in-plane π orbitals. This supports the presence of the long-range interaction regions in the kinetic energy densities, though this has yet to be fully established.

The effects of the PSRSIC on the electron density is also drawn in Fig. 2. Note that the LC has often been interpreted to modify one-electron self-interaction errors, which cause poor orbital energies.[39] Since the PSRSIC in Sec. 2.2 is a correction only for the one-electron self-interaction, the correlation of the LC and one-electron self-interaction corrections is figured out by looking into the PSRSIC effect on electron density. The figure shows that the self-interaction regions where the PSRSIC stabilises, the reddish regions pointed in the solid lines of the second right plots, are much broader for the core regions and hardly cover the hydrogen atoms than those of t_σ, the reddish regions shown in the solid lines of the left plots. This seems inconsistent with the formulation of the PSRSIC, because the PSRSIC is the correction only for the regions of t_σ larger than a threshold.[41] However, this is attributed to the relative sizes of the pseudospectral exchange energy density and the exchange energy density of the substituted uncorrected DFT exchange functional for each atom. The regions of larger exchange energy density accommodate more electrons. Therefore, the pseudospectral exchange energy density is smaller than that of the uncorrected exchange functional for hydrogen atom, while the former is larger than the latter for the core orbitals of oxygen and carbon atoms. This is because the Becke 1988 exchange functional and other conventional exchange functionals generally contain parallel-spin electron correlations.[56] As a result, this exchange functional overestimates exchange energy for hydrogen atoms, because hydrogen atom contains only the opposite-spin electron correlation between the electrons in the same orbital. Therefore, the plots of the PSRSIC do not completely correspond to the self-interaction regions for the hydrogen atoms. Comparing the LC and PSRSIC effects shows that these effects similarly move electrons from around hydrogen atoms to the valence electron regions of carbon and oxygen atoms in the molecular planes. However, these effects are dissimilar for long-range interaction regions far from σ bonds in the molecular planes and are opposite for long-range interaction regions in the vertical planes. This indicates that the long-range interaction regions are the regions where the LC excluding its self-interaction correction parts stabilizes electrons.

Figure 2 also illustrates the CCSD effects on total electron density, which are calculated as the difference between the CCSD electron densities and the BLYP ones. Interestingly, these effects suggest the corrections for the electron densities that should be incorporated in the DFT functionals. The figure shows that the CCSD effects increase the electron densities near the bonds and decrease them in the self-interaction regions except for the deepest core

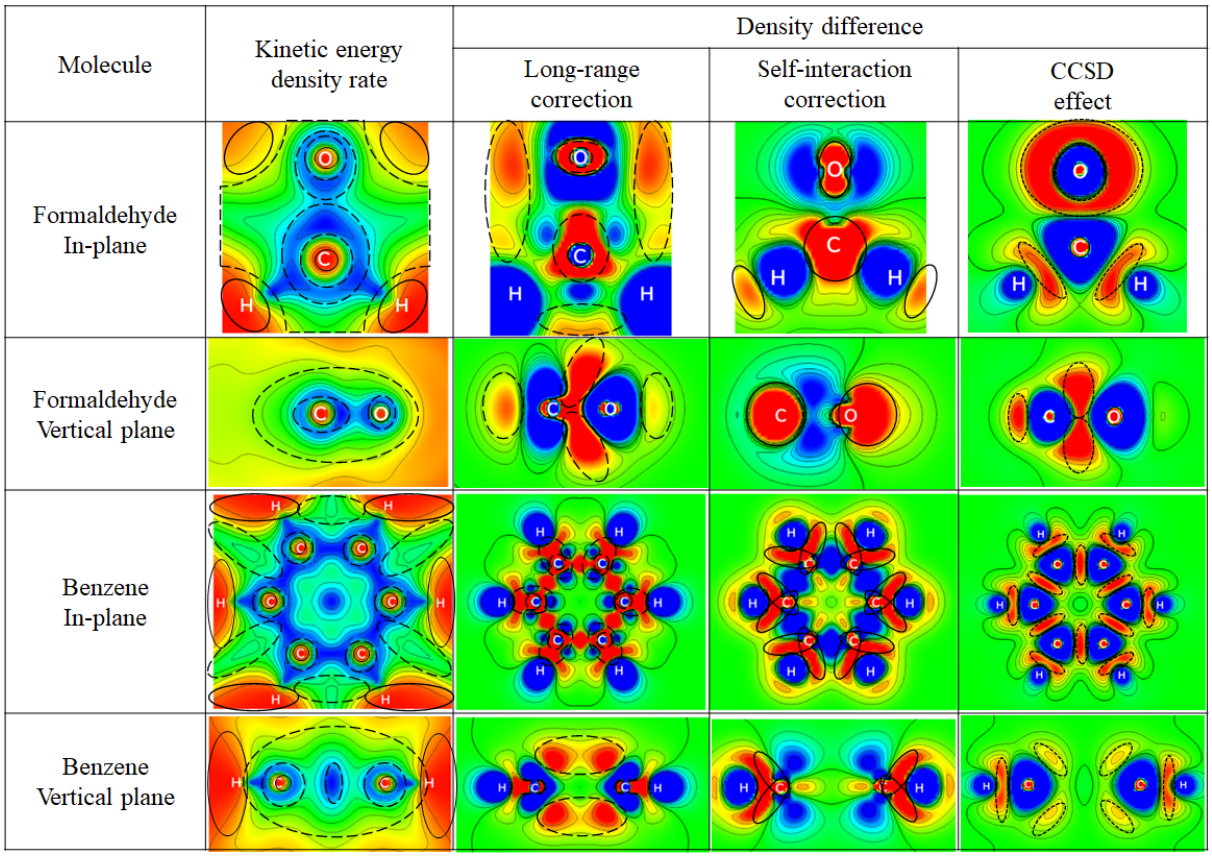

Figure 2: Contour plots of three total density differences, the differences of LC-BLYP and BLYP in the column of "Long-range correction", LC-PSRSIC-BLYP and LC-BLYP in the column of "Self-interaction correction", and CCSD and BLYP in the column of "CCSD effect", for the electronic states of formaldehyde and benzene molecules in the molecular in-planes and vertical planes. The plot ranges of the density differences are from -0.0008 to $+0.0008$ (formaldehyde) and -0.001 to $+0.001$ (benzene) for the long-range correction and from -0.003 to $+0.003$ (formaldehyde) and -0.002 to $+0.002$ (benzene) for the self-interaction correction, and from -0.003 to $+0.003$ (formaldehyde) and -0.0025 to $+0.0025$ (benzene) and the CCSD effect in the unit of e/(a.u.)^3. For comparison, the contour plots of the kinetic energy density ratio, $t_\sigma = \tau_\sigma^{\rm W}/\tau_\sigma^{\rm total}$ $(0 \leq t_\sigma \leq 1)$ in Eq. (3), are also shown in the column of "Kinetic energy density ratio". The colour levels are drawn to have ten equal parts for all the contour plots. The dashed lines roughly surround the long-range interaction regions of kinetic energy density, while the solid and dotted lines approximately draw round regions where the PSRSIC and the CCSD effect stabilise electrons, respectively. Both the kinetic energy density ratio and density difference increase in the order of blue, green, and red.

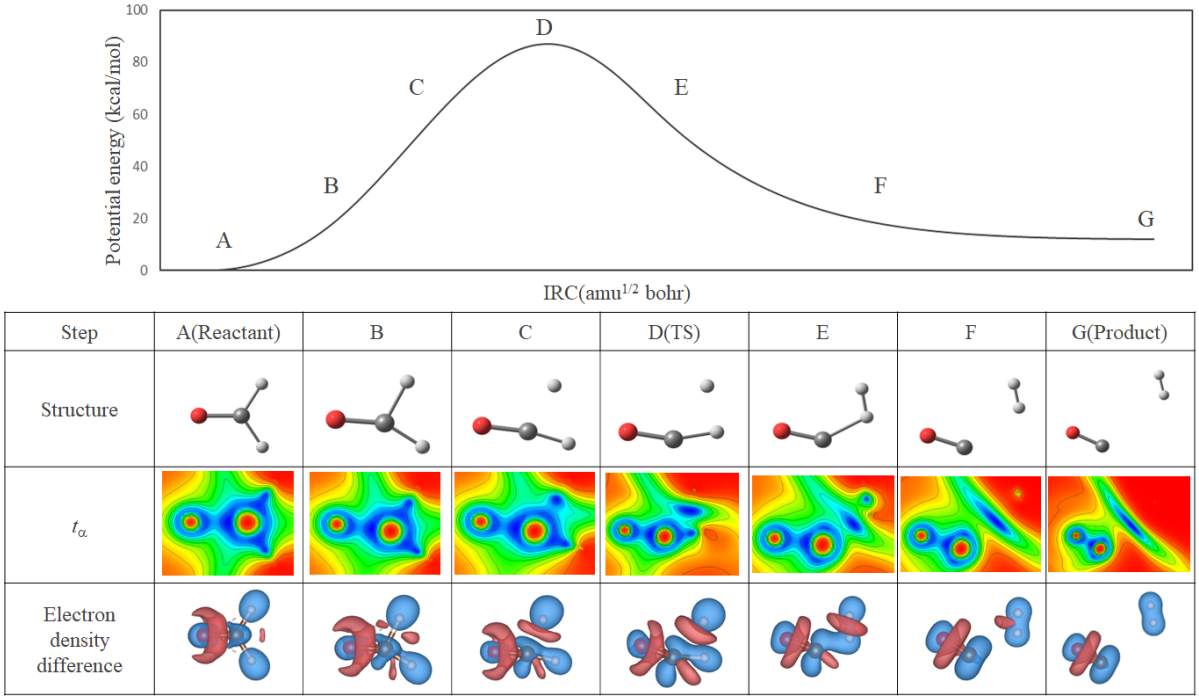

Figure 3: Contour plots of the variation of the α-spin kinetic energy density rate t_α in Eq. (3) at "t_α" and the LC effect on the electron density (the signed difference between the LC-BLYP and BLYP electron densities) at "Electron density difference", with their molecular structures at "Structure" for the steps on the IRC of the dissociation reaction of formaldehyde molecule to the carbon monoxide and hydrogen molecules, which are calculated using LC-BLYP/aug-cc-pVTZ method. The colour levels of t_α ($0 \leq t_\alpha \leq 1$) are drawn to have ten equal parts. In the figures of the electron density differences, the red and blue regions indicate the increasing (plus) and decreasing (minus) electron density parts by the LC effect, respectively. The potential energy curve of this IRC is shown at the top.

regions. Notably, the CCSD effects are similar to the LC effects for the electron densities in the vertical planes. However, they do not affect the densities in the long-range interaction regions of the LC in the molecular planes. These results indicate that the pure BLYP functional is insufficient for the long-range exchange effects on the electrons in the regions perpendicular to the σ bonds and the electron correlation effects on the electrons near the σ bonds.

4.2 Long-range interaction regions in reactions

Next, the long-range interaction regions of the LC in reactions are examined to clarify the long-range exchange effects on the reactions.

Figure 3 shows the kinetic energy density ratio in Eq. (3) and the LC effect on electron density for the dissociation reaction of formaldehyde molecule into carbon monoxide and hydrogen molecules: $HCHO \rightarrow CO + H_2$. As shown in the contour plots of kinetic energy

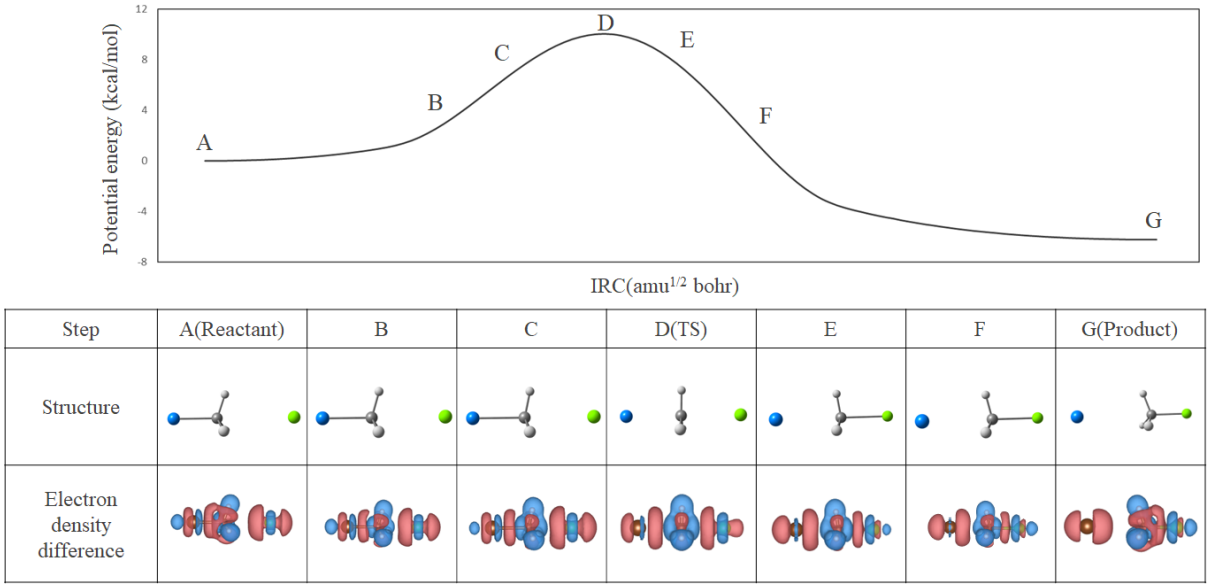

Figure 4: Variations in the LC effect on the electron density (the signed difference between the LC-BLYP and BLYP electron densities) at "Electron density difference" and their molecular structures at "Structure" for the steps on the IRC of the S_N2 reaction of bromomethane and chlorine to chloromethane and bromine, which are calculated using LC-BLYP/aug-cc-pVTZ method. In the figures of the electron density differences, the red and blue regions indicate the increasing (plus) and decreasing (minus) electron density parts by the LC effect, respectively. The potential energy curve of this IRC is also shown at the top.

density rate, the long-range interaction regions of the LC move and stay around the perpendicular regions of the dissociating σ bond between hydrogen and carbon monoxide molecules. Note that hydrogen molecule disappears in the plot of the product (G), because it contains only self-interacting electrons. Although the long-range interaction regions of the LC are also found around the dissociating bond, they then move to the π orbitals of the dissociated molecules. This discrepancy derives from the absence of electrons in the perpendicular regions of the dissociating H_2-CO bond, which leads to the disappearance of the electron density variance even for the strong long-range exchange effect. Therefore, the long-range interaction regions are similar for the kinetic energy and electron density differences.

Next, the long-range interaction regions of the LC for other reactions are investigated. Figure 4 shows the long-range interaction regions of the LC based on electron density for the S_N2 reaction of Cl + $CH_3Br \rightarrow ClCH_3$ + Br. As shown in the figure, the long-range interaction regions of the LC are found at the p_z orbitals of Br and Cl atoms located on the reaction axis (z). The long-range interaction regions of the LC in the S_N2 reaction are precisely the regions perpendicular to the molecular axis, similar to that of the previous dissociation reaction of formaldehyde. Figure 5 illustrates the LC effect on electron density in the Diels-Alder reaction of butadiene and ethylene to cyclohexene. The figure indicates that the long-range interaction regions spread over the π orbital of butadiene toward ethylene through electron transfers from the core orbitals and finally expand to the regions perpen-

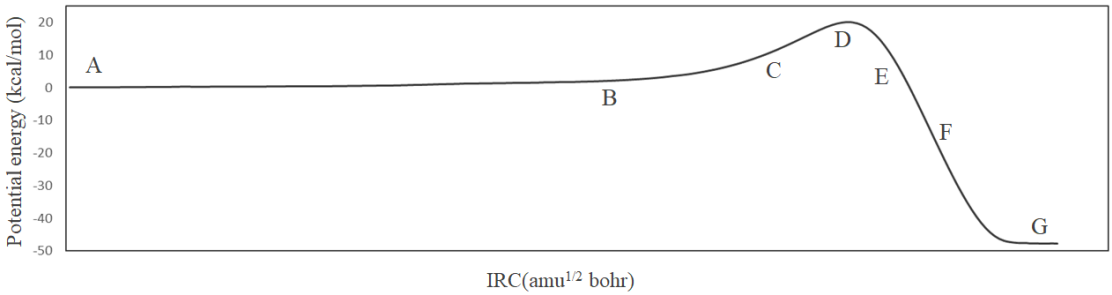

Step	A(Reactant)	B	C	D(TS)	E	F	G(Product)
Structure							
Electron density difference							

Figure 5: Variation in the LC effect on the electron density, the signed difference between the LC-BLYP and BLYP electron densities at "Electron density difference" and their molecular structures at "Structure" for the steps on the IRC of the Diels-Alder reaction of butadiene and ethylene to cyclohexene with the structure at each step, which are calculated using LC-BLYP/aug-cc-pVTZ method. In the figures of the electron density differences, the red and blue regions indicate the increasing (plus) and decreasing (minus) electron density parts by the LC effect, respectively. The potential energy curve of this IRC is also shown at the top.

dicular to the σ bonds. Thus, the long-range interaction regions of the LC mediate the bond formations.

In summary, the long-range interaction regions of the LC are present around the formed and dissociated bonds to mediate the reactions, similar to those of the kinetic energy density, through the electron transfers from core orbitals to the bonding π orbitals.

4.3 Long-range interaction regions in orbital densities

Although the effects on total electron density have, so far, been targeted, it is more precise to test DFT functionals for the reproducibility of one-electron density, which is the electron density of molecular orbital. This is because the Hohenberg-Kohn theorem[20] establishes the mapping to one-electron external potential, which directly acts on one-electron density, i.e., orbital density. From a practical viewpoint, it is also significant to indicate that the reproducibility of response properties, which are dominant in chemical properties, is essentially determined by molecular orbitals and orbital energies. According to the linear response theory[57] for calculating response properties, defining the response function of the electron density χ for the infinitesimal change in the potential δv as,

$$\delta\rho(\mathbf{r}_1, t_1) = \iint dt_2 d^3\mathbf{r}_2 \chi[\rho_0](\mathbf{r}_1, \mathbf{r}_2, t_2 - t_1)\delta v(\mathbf{r}_2, t_2), \tag{18}$$

where ρ_0 is the nonvariational part of density, leads to the response function in the form of the Fourier transformation (time $t \rightarrow$ frequency ω) as

$$\chi(\mathbf{r}_1, \mathbf{r}_2, \omega) = 2 \lim_{\eta \to 0+} \sum_{i}^{n_{\mathrm{occ}}} \sum_{a}^{n_{\mathrm{unocc}}} \left[\frac{\phi_i^*(\mathbf{r}_1)\phi_a(\mathbf{r}_1)\phi_i(\mathbf{r}_2)\phi_a^*(\mathbf{r}_2)}{\omega - (\epsilon_a - \epsilon_i) + i\eta} - \frac{\phi_i(\mathbf{r}_1)\phi_a^*(\mathbf{r}_1)\phi_i^*(\mathbf{r}_2)\phi_a(\mathbf{r}_2)}{\omega + (\epsilon_a - \epsilon_i) - i\eta} \right], \tag{19}$$

where ϕ_i and ϕ_a are occupied and unoccupied molecular orbitals, ϵ_i and ϵ_a are the corresponding orbital energies, and n_{occ} and n_{unocc} are the number of the occupied and unoccupied orbitals. It is, therefore, reasonable to explore the LC effect on orbital densities to reveal the cause for the accurate orbital energies of LC-DFT.[12] In the conventional self-interaction correction,[58,59] the orbital density is assumed to have the representability of potential v, similar to total electron density in the Hohenberg-Kohn theorem.[20] Therefore, it is meaningful to display the long-range interaction regions of the LC in the orbital densities by comparing to the Dyson orbital densities of CCSD wavefunctions.

Figure 6 illustrates the density differences of the canonical orbitals for LC-BOP and BOP with the orbital energies of LC-BOP for formaldehyde. As shown in the figure, the long-range interaction regions depend on the orbitals as being opposite for HOMO−3 and HOMO and for LUMO and LUMO+4. The figure also displays the canonical orbital energies of LC-BOP with the minus ionisation potentials and electron affinities of the CCSD calculations, which correspond to the occupied and unoccupied orbital energies of the CCSD Dyson orbitals. The long-range interaction regions cannot explain the general trend that the LC lowers the occupied orbital energies and raises the unoccupied ones. In particular, the long-range interaction regions of orbital densities hardly affect the improvement of the calculated orbital energies.

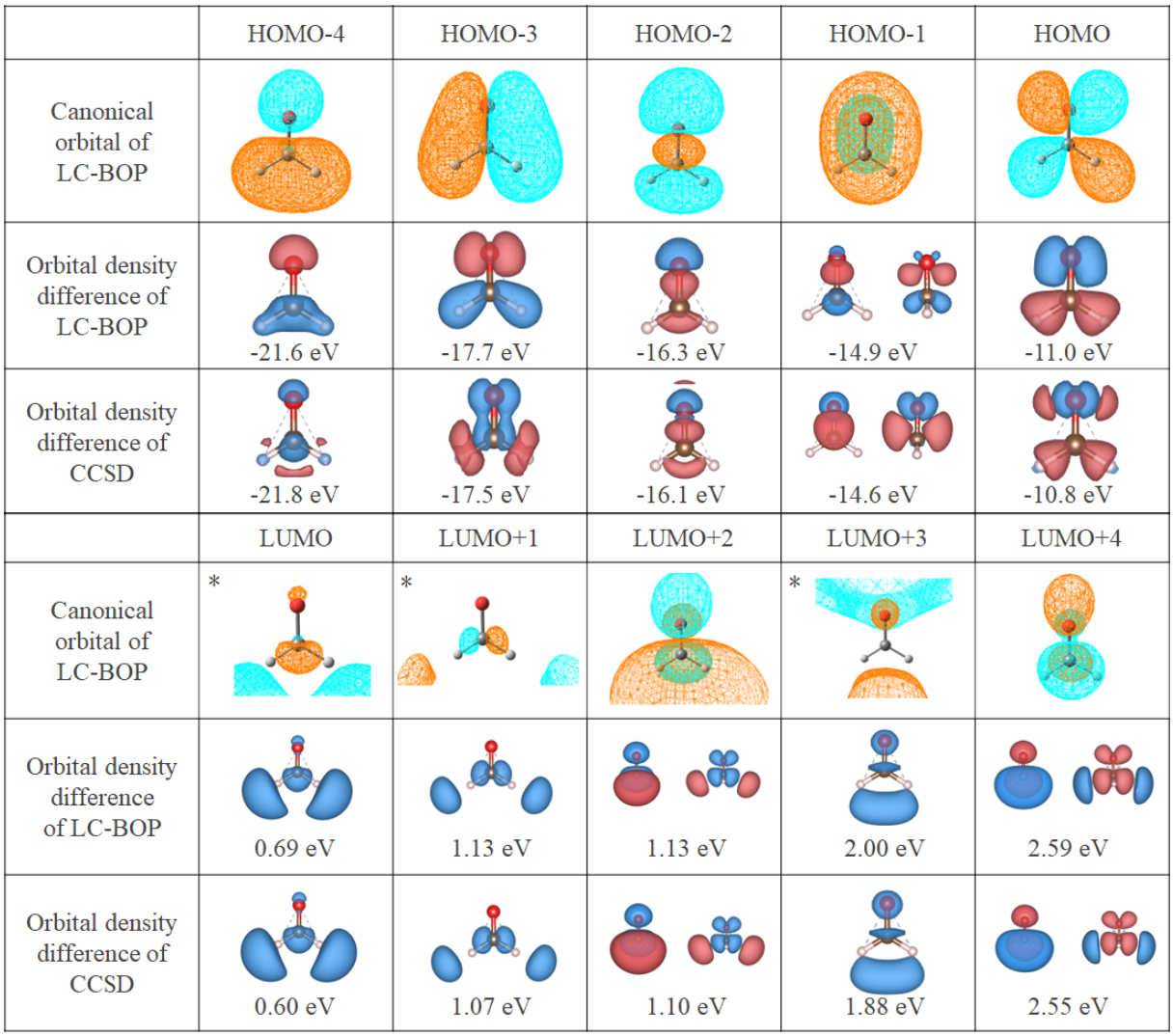

Figure 6: The LC and CCSD effects on the orbital densities of formaldehyde molecule and their orbital images for HOMO−5 through LUMO+5, which are calculated with the aug-cc-pVTZ basis set. These effects are calculated as the electron density differences of the LC-BOP canonical orbitals and CCSD Dyson orbitals from the corresponding BOP canonical orbitals. For the orbital densities, the red and blue parts indicate the increasing (plus) and decreasing (minus) densities, respectively. The orbital energies of the canonical orbitals and the minus ionisation potentials and electron affinities corresponding to the occupied and unoccupied Dyson orbitals, respectively, are also attached. The threshold for the drawing is 0.03 e/au^3 for the canonical orbital images except the asterisk mark-attached ones (0.025 e/au^3), while in the case of the density difference images, it is 0.0005 e/au^3 for the occupied orbitals and 0.0006 e/au^3 for the unoccupied orbitals.

In Fig. 6, the density differences of the CCSD Dyson orbital densities from the corresponding BOP canonical orbital densities are also shown for formaldehyde. Compared to the orbital density differences of LC-BOP, the CCSD effects on the orbital densities have different shapes for the occupied orbitals, although they are similar to each other for the unoccupied orbitals. Interestingly, this result indicates that the long-range exchange effects dominate the CCSD effects on the unoccupied orbitals, while the electron correlation effects are significant in those of the occupied orbitals. It should be emphasised that although only the canonical orbitals of LC-BOP are shown in the figure, approximately the same orbital shapes are given for the CCSD Dyson orbitals with the corresponding closer orbital energies. As discussed for the effects on the total electron densities, the CCSD effects mainly contribute to the stabilisation of the bonds and the destabilisation of electrons in the self-interaction regions. This result is consistent with this discussion. However, similar orbital shapes are given with significantly small differences for the LC-BOP canonical and CCSD Dyson orbitals with closer orbital energies.

The long-range interaction regions of orbital densities are also examined for benzene molecule. In Fig. 7, the orbital density variations by the LC are illustrated. The long-range interaction regions of orbital densities are found around in-plane π orbitals of the ring for the occupied orbitals, and around hydrogen atoms outside the ring for the unoccupied orbitals. However, explaining the relation of these regions with the orbital energies is difficult, because the types of the orbitals covering these regions are different. Therefore, the long-range interaction regions of orbital densities are not associated with improving the orbital energies.

Figure 7 also shows that the CCSD effects on the orbital densities mainly derived from the long-range exchange effects for benzene molecule. As shown in the figure, similar orbital density differences are provided for the LC-BOP and CCSD effects except for HOMO$-$1, HOMO, LUMO+3, and LUMO+4. The differences in these orbital densities come from the shapes of the CCSD Dyson orbitals. The Dyson orbitals seem to mix at a specific ratio from the LC-BOP ones (Fig. 8). This result is attributable to the determination method of the Dyson orbitals, because the Dyson orbitals are determined using the wavefunctions of the cations and anions, as shown in Eqs. (13) and (14), in which the degenerate orbitals of the neutrals are mixed in the ions after removing or adding one of them. Consequently, HOMOs become mixed in these degenerate orbitals. For other orbitals, the Dyson orbitals provide approximately the same orbital shapes as those of the corresponding canonical orbitals, while the corresponding orbital energies are sufficiently close to each other even for these orbitals. These results suggest the long-range exchange effects dominate the CCSD effects on the orbital densities of benzene from those of the pure BOP functional. However, the degenerate orbitals of the neutrals are mixed in the Dyson orbitals.

These orbital density analyses raise questions regarding the fundamental concept of DFT that the quality of the DFT functional should be verified by the calculated total electron density, because these analyses also reveal the shortcomings of DFT functional compared to the CCSD method. The orbitals are the solution of the Kohn-Sham equation and usually determine the quality of the calculated chemical properties. In addition, the accuracy of orbital energies is determined by neither the exchange-correlation energy E_{xc} nor potential v_{xc} but the exchange-correlation integral kernel $f_{\mathrm{xc}} = \delta v_{\mathrm{xc}}/\delta\rho$.[12] Therefore, even a sophisticated exchange-correlation potential cannot provide accurate orbital energies and the correspond-

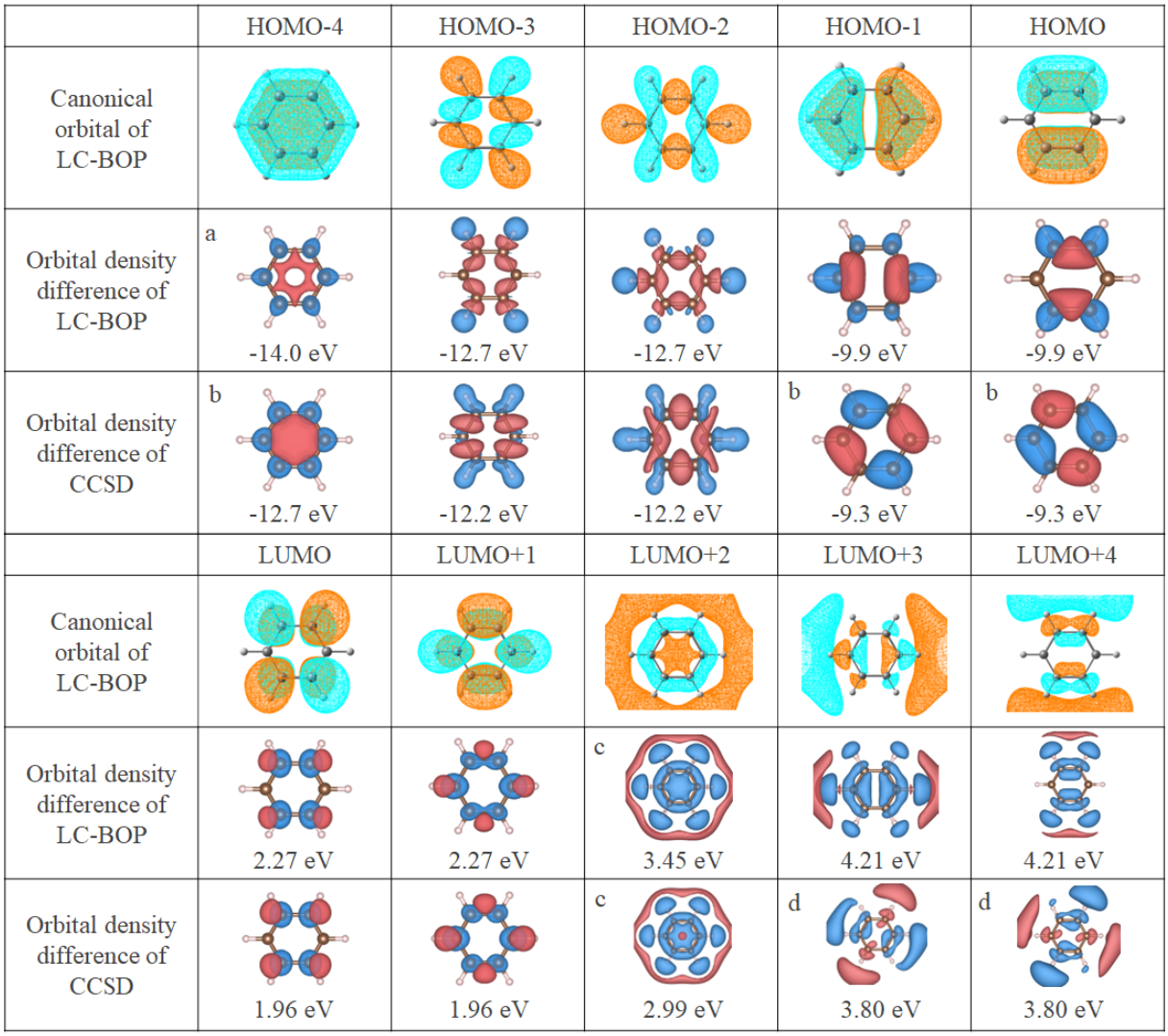

Figure 7: The LC and CCSD effects on the orbital densities of benzene molecule with their orbital images for HOMO−5 through LUMO+5, which are calculated with the cc-pVTZ basis set. The effects are calculated as the density differences of the LC-BOP canonical orbitals and CCSD Dyson orbitals from the corresponding BOP canonical orbitals. For the orbital densities, the red and blue parts indicate the increasing and decreasing densities, respectively. The orbital energies of the canonical orbitals and the minus ionisation potentials and electron affinities corresponding to the occupied and unoccupied Dyson orbitals, respectively, are also attached. The threshold for the drawing is 0.03 e/au^3 for the canonical orbital images. For the density difference images, the threshold for the drawing is 0.0001 e/au^3 for the occupied orbitals and 0.0003 e/au^3 for the unoccupied orbitals, while the thresholds for the a, b, c, and d-attached orbital density difference images are 0.000035, 0.0002, 0.00015 and 0.001 e/au^3, respectively.

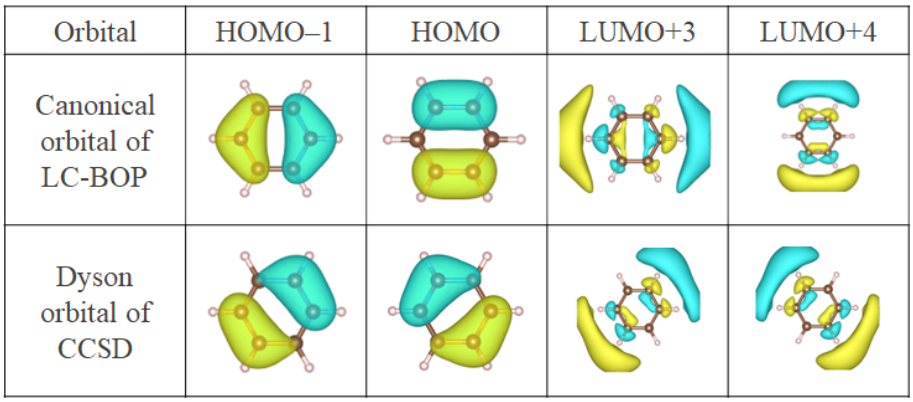

Figure 8: The Dyson orbitals of the CCSD wavefunction and the canonical Kohn-Sham orbitals of LC-BOP of benzene molecule, which are calculated with the cc-pVTZ basis set, for the orbitals of the inconsistent shapes.

ing orbitals, for the unoccupied orbitals.[60] The present results confirm that orbital densities are available for more precisely exploring the quality of DFT functionals.

4.4 Photoionisation cross section calculations

Finally, the photoionisation cross sections are calculated as a direct examination for the molecular orbital shapes. As reviewed in Sec. 2.3, the photoionisation cross sections essentially depend only on the HOMO shapes. The cross section calculations can directly examine the HOMO densities, because the HOMO density is the square of the HOMO.

Figure 9 illustrates the total photoionisation cross sections with respect to the ionising radiation energy in the energy ranges around the HOMO energies. Note that the experimental cross sections should be compared as a reference, because they essentially have wide error bars. Therefore, it is reasonable to consider that the calculated photoionisation cross sections of the CCSD Dyson orbitals are more reliable than the experimental ones in the framework of the calculations. As shown in the figure, LC-BOP canonical HOMOs provide close cross sections to those of the CCSD Dyson HOMOs for formaldehyde, water, and cyclopentene. These cross sections are close to the experimental ones.[61–63] In contrast, the cross sections of the HF and BOP canonical HOMOs are inconsistent for these molecules, and give relatively large discrepancies from the experimental ones. These results clearly indicate that the photoionisation cross sections are available as a direct examination for the orbital shapes, and LC-BOP canonical and CCSD Dyson HOMOs are close to the real ones.

However, as shown in Fig. 9(c), the photoionisation cross sections of benzene molecule provide different behaviors: the cross section of the LC-BOP canonical HOMO is close to that of the BOP canonical HOMO, and it is much smaller than that of the CCSD Dyson HOMO. This difference can be explained by the different shapes of the HOMO of the benzene molecule for at least low ionising radiation energy, as discussed in Sec. 4.3. As shown in Fig. 8, the CCSD Dyson HOMO has a shape different from the canonical HOMO of LC-BOP due to the mixing with HOMO−1. The photoionisation cross section in Eq. (16) depends only

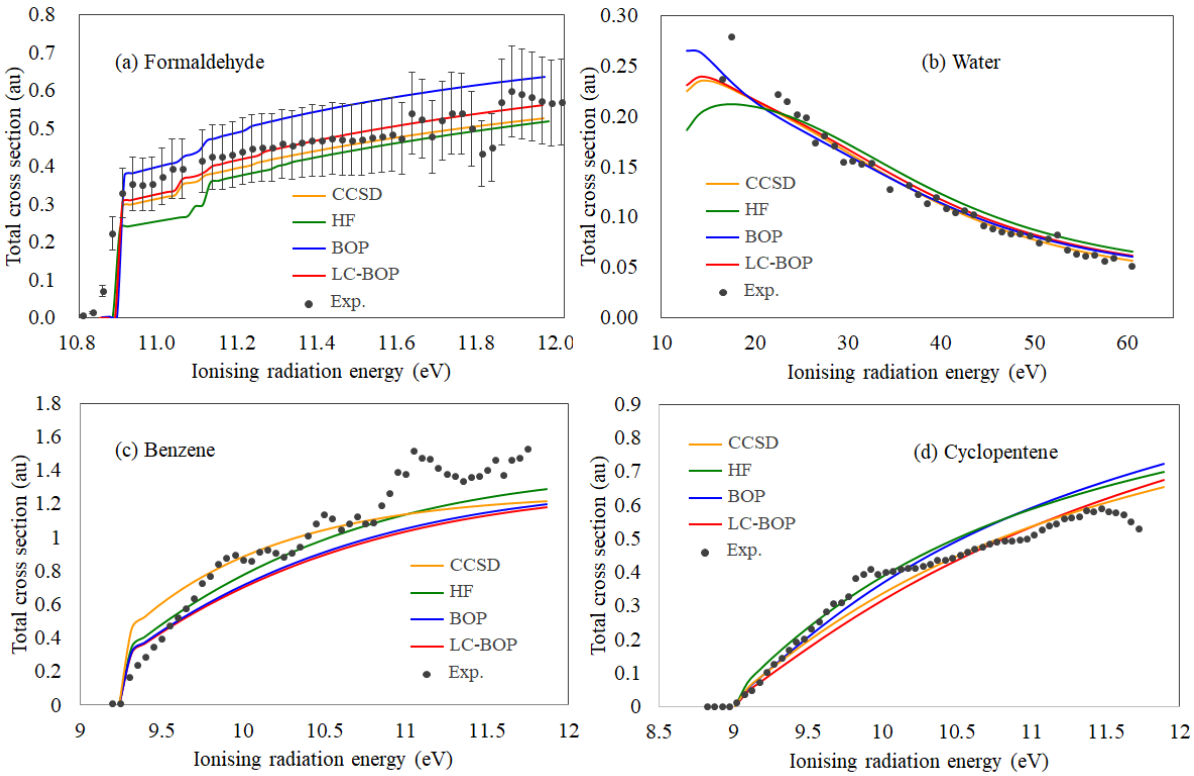

Figure 9: Photoionisation cross sections of four molecules, (a) formaldehyde, (b) water, (c) benzene and (d) cyclopentene molecules, in terms of the ionising radiation energy in the energy range around each HOMO energy. In the calculations of the cross sections, the HF, BOP, and LC-BOP canonical HOMOs and the CCSD Dyson HOMOs of these molecules, which are calculated with the aug-cc-pVTZ basis set for formaldehyde, water, and cyclopentene and cc-pVTZ basis set for benzene, are used. The experimental cross sections[61–63] are also shown as black dots.

on the shape of HOMO. In this figure, the calculated cross sections of LC-BOP and BOP are found to be closer to the experimental ones than those of the CCSD and HF methods for small ionising radiation energy, while the latter ones are closer than the former ones for large ionising radiation energy. However, note that since the behaviours of the calculated cross sections are different from the experimental ones as a whole, there is room for further investigation of the cross sections of the benzene molecule.

In summary, the photoionisation cross sections of the LC-BOP canonical orbitals are close to those of the CCSD Dyson orbitals except for the benzene molecule. Since the CCSD Dyson orbitals are directly extracted from the CCSD wavefunctions containing high-level electron correlations, the closely calculated cross sections of the LC-BOP canonical orbitals imply that LC-BOP canonical orbitals incorporate high-level electron correlations.

5 Conclusions

In this study, we have comparatively investigated the effects of the long-range correction (LC) and the *ab initio* CCSD method on total and one-electron orbital densities to clarify the long-range interaction regions of molecules and for revealing the LC effect on the molecular orbitals from the viewpoint of the orbital shapes.

We discovered that the long-range interaction regions of the LC, where the LC increases electron densities, well overlap with those of the kinetic energy density, which were assumed to appear outside the free electron and self-interaction regions. Furthermore, we found that the CCSD method increases the electron densities of the long-range interaction regions in the vertical molecular planes. However, it also increases the in-plane electron densities near the bonds. We next explored the long-range interaction regions in the total electron densities for the IRCs of three reactions: i.e., the dissociation reaction of formaldehyde, the S_N2 reaction of bromomethane and chlorine, and the Diels-Alder reaction of butadiene and ethylene. Consequently, we found that the long-range interaction regions appear in the middle of the formed bond and then spread into the regions perpendicular to the σ bonds in the reaction processes.

Following the analysis of total electron density, we discussed the one-electron orbital density compared to the effects on the Dyson orbital density of the CCSD wavefunction. Note that this analysis is more important than that of total electron density, because most chemical properties directly depend on the orbitals. Surprisingly, we found that no significant differences between the LC and CCSD effects are given for the unoccupied orbitals, indicating that the long-range exchange effects dominate the CCSD effects on the unoccupied orbitals. The effects on the occupied orbitals contrastingly lack consistency and seem unrelated to the long-range interaction regions of total electron density. To explore this inconsistency, we calculated the photoionisation cross sections using the canonical Kohn-Sham and CCSD Dyson HOMOs as a direct test for the orbital densities. Consequently, we found that the LC makes the HOMOs close to the CCSD ones, whereas in case of only for benzene, the LC and CCSD results differ significantly due to the mixing of the degenerate HOMO-1 in the CCSD Dyson HOMO. These results propose that the orbital analyses using the photoionisation cross sections are available as a direct test for the quality of DFT functionals and the LC-DFT canonical orbitals incorporate similar high-level electron correlations to those of the CCSD Dyson orbitals.

Acknowledgments

This research was financially supported by JST CREST, Japan (Grant No. JPMJCR1902). A part of calculations was performed using Research Center for Computational Science, Okazaki, Japan (Project: 22-IMS-C019).

Supporting Information Available

The calculated canonical LC-BOP and CCSD Dyson molecular orbitals are illustrated for the five highest occupied (Fig. S1) and five lowest unoccupied (Fig. S2) orbitals of formaldehyde

molecule and for the five highest occupied (Fig. S3) and five lowest unoccupied (Fig. S4) orbitals of benzene molecule in the supporting information file.

Figure Captions

Fig. 1. Contour plot of the ratio of the von Weizsäcker kinetic energy density to the total one, t_σ ($0 \leq t_\sigma \leq 1$) in Eq. (3), for the electronic state of the furan molecule. The colour levels are drawn to have ten equal parts. In the plot, the red regions, where t_σ is close to one, indicate the self-interaction regions, while the blue regions, where t_σ is close to zero, show the free-electron regions. The remaining green regions are called long-range interaction regions.

Fig. 2. Contour plots of three total density differences, the differences of LC-BLYP and BLYP in the column of "Long-range correction", LC-PSRSIC-BLYP and LC-BLYP in the column of "Self-interaction correction", and CCSD and BLYP in the column of "CCSD effect", for the electronic states of formaldehyde and benzene molecules in the molecular in-planes and vertical planes. The plot ranges of the density differences are from -0.0008 to $+0.0008$ (formaldehyde) and -0.001 to $+0.001$ (benzene) for the long-range correction and from -0.003 to $+0.003$ (formaldehyde) and -0.002 to $+0.002$ (benzene) for the self-interaction correction, and from -0.003 to $+0.003$ (formaldehyde) and -0.0025 to $+0.0025$ (benzene) and the CCSD effect in the unit of e/(a.u.)^3. For comparison, the contour plots of the kinetic energy density ratio, $t_\sigma = \tau_\sigma^{\mathrm{W}}/\tau_\sigma^{\mathrm{total}}$ ($0 \leq t_\sigma \leq 1$) in Eq. (3), are also shown in the column of "Kinetic energy density ratio". The colour levels are drawn to have ten equal parts for all the contour plots. The dashed lines roughly surround the long-range interaction regions of kinetic energy density, while the solid and dotted lines approximately draw round regions where the PSRSIC and the CCSD effect stabilise electrons, respectively. Both the kinetic energy density ratio and density difference increase in the order of blue, green, and red.

Fig. 3. Contour plots of the variation of the α-spin kinetic energy density rate t_α in Eq. (3) at "t_α" and the LC effect on the electron density (the signed difference between the LC-BLYP and BLYP electron densities) at "Electron density difference", with their molecular structures at "Structure" for the steps on the IRC of the dissociation reaction of formaldehyde molecule to the carbon monoxide and hydrogen molecules, which are calculated using LC-BLYP/aug-cc-pVTZ method. The colour levels of t_σ are drawn to have ten equal parts. In the figures of the electron density differences, the reddish and blueish regions indicate the increasing (plus) and decreased (minus) electron density parts by the LC effect, respectively. The potential energy curve of this IRC is shown at the top.

Fig. 4. Variations in the LC effect on the electron density (the signed difference between the LC-BLYP and BLYP electron densities) at "Electron density difference" and their molecular structures at "Structure" for the steps on the IRC of the S_N2 reaction of bromomethane and chlorine to chloromethane and bromine, which are calculated using LC-BLYP/aug-cc-pVTZ method. In the figures of the electron density differences, the reddish and blueish regions indicate the increasing (plus) and decreased (minus) electron density parts by the LC effect, respectively. The potential energy curve of this IRC is also shown at the top.

Fig. 5. Variation in the LC effect on the electron density, the signed difference between the

LC-BLYP and BLYP electron densities at "Electron density difference" and their molecular structures at "Structure" for the steps on the IRC of the Diels-Alder reaction of butadiene and ethylene to cyclohexene with the structure at each step, which are calculated using LC-BLYP/aug-cc-pVTZ method. In the figures of the electron density differences, the reddish and blueish regions indicate the increasing (plus) and decreased (minus) electron density parts by the LC effect, respectively. The potential energy curve of this IRC is also shown at the top.

Fig. 6. The LC and CCSD effects on the orbital densities of formaldehyde molecule and their orbital images for HOMO−5 through LUMO+5, which are calculated with the aug-cc-pVTZ basis set. These effects are calculated as the electron density differences of the LC-BOP canonical orbitals and CCSD Dyson orbitals from the corresponding BOP canonical orbitals. For the orbital densities, the red and blue parts indicate the increasing and decreasing densities, respectively. The orbital energies of the canonical orbitals and the minus ionisation potentials and electron affinities corresponding to the occupied and unoccupied Dyson orbitals, respectively, are also attached. The threshold for the drawing is 0.03 e/au^3 for the canonical orbital images except the asterisk mark-attached ones (0.025 e/au^3), while in the case of the density difference images, it is 0.0005 e/au^3 for the occupied orbitals and 0.0006 e/au^3 for the unoccupied orbitals.

Fig. 7. The LC and CCSD effects on the orbital densities of benzene molecule with their orbital images for HOMO−5 through LUMO+5, which are calculated with the cc-pVTZ basis set. The effects are calculated as the density differences of the LC-BOP canonical orbitals and CCSD Dyson orbitals from the corresponding BOP canonical orbitals. For the orbital densities, the red and blue parts indicate the increasing and decreasing densities, respectively. The orbital energies of the canonical orbitals and the minus ionisation potentials and electron affinities corresponding to the occupied and unoccupied Dyson orbitals, respectively, are also attached. The threshold for the drawing is 0.03 e/au^3 for the canonical orbital images. For the density difference images, the threshold for the drawing is 0.0001 e/au^3 for the occupied orbitals and 0.0003 e/au^3 for the unoccupied orbitals, while the thresholds for the a, b, c, and d-attached orbital density difference images are 0.000035, 0.0002, 0.00015 and 0.001 e/au^3, respectively.

Fig. 8. The Dyson orbitals of the CCSD wavefunction and the canonical Kohn-Sham orbitals of LC-BOP of benzene molecule, which are calculated with the cc-pVTZ basis set, for the orbitals of the inconsistent shapes.

Fig. 9. Photoionisation cross sections of four molecules, (a) formaldehyde, (b) water, (c) benzene and (d) cyclopentene molecules, in terms of the ionising radiation energy in the energy range around each HOMO energy. In the calculations of the cross sections, the HF, BOP, and LC-BOP canonical HOMOs and the CCSD Dyson HOMOs of these molecules, which are calculated with the aug-cc-pVTZ basis set for formaldehyde, water, and cyclopentene and cc-pVTZ basis set for benzene, are used. The experimental cross sections[61–63] are also shown as black dots.

References

[1] T. Tsuneda and K. Hirao, *WIREs Comput. Mol. Sci.*, 2014, **4**, 375–390.

[2] H. Iikura, T. Tsuneda, T. Yanai and K. Hirao, *J. Chem. Phys.*, 2001, **115**, 3540–3544.

[3] T. Yanai, D. P. Tew and N. C. Handy, *Chem. Phys. Lett.*, 2004, **91**, 51–57.

[4] O. A. Vydrov, J. Heyd, A. Krukau and G. E. Scuseria, *J. Chem. Phys.*, 2006, **125**, 074106(1–9).

[5] J.-D. Chai and M. Head-Gordon, *J. Chem. Phys.*, 2008, **128**, 084106(1–15).

[6] R. Baer, E. Livshits and U. Salzner, *Annu. Rev. Phys. Chem.*, 2010, **61**, 85–109.

[7] Y. Tawada, T. Tsuneda, S. Yanagisawa, T. Yanai and K. Hirao, *J. Chem. Phys.*, 2004, **120**, 8425–8433.

[8] M. Kamiya, H. Sekino, T. Tsuneda and K. Hirao, *J. Chem. Phys.*, 2005, **122**, 234111(1–10).

[9] R. Kishi, S. Bonness, K. Yoneda, H. Takahashi, M. Nakano, E. Botek, B. Champagne, T. Kubo, K. Kamada, K. Ohta and T. Tsuneda, *J. Chem. Phys.*, 2010, **132**, 094107(1–11).

[10] A. K. Lihua Xu and B. M. Wong, *J. Comput. Chem.*, 2018, **39**, 2350–2359.

[11] P. Besalú-Sala, S. P. Sitkiewicz, P. Salvador, E. Matito and J. M. Luis, *Phys. Chem. Chem. Phys.*, 2020, **22**, 11871–11880.

[12] T. Tsuneda, J.-W. Song, S. Suzuki and K. Hirao, *J. Chem. Phys.*, 2010, **133**, 174101(1–9).

[13] A. Nakata and T. Tsuneda, *J. Chem. Phys.*, 2013, **139**, 064102(1–9).

[14] T. Tsuneda and R. K. Singh, *J. Comput. Chem.*, 2014, **35**, 1093–1100.

[15] T. Tsuneda, H. Sumitomo, M. Hasebe, T. Tsutsumi and T. Taketsugu, *J. Comput. Chem.*, 2023, **44**, 93–104.

[16] M. Hasebe, T. Tsutsumi, T. Taketsugu and T. Tsuneda, *J. Chem. Theory Comput.*, 2021, **17**, 6901–6909.

[17] M. G. Medvedev, I. S. Bushmarinov, J. Sun, J. P. Perdew and K. A. Lyssenko, *Science*, 2017, **355**, 49–52.

[18] X. Andrade and A. Aspuru-Guzik, *Phys. Rev. Lett.*, 2011, **107**, 183002(1–5).

[19] E. Sim, S. Song and K. Burke, *J. Phys. Chem. Lett.*, 2018, **9**, 6385–6392.

[20] P. Hohenberg and W. Kohn, *Phys. Rev. B*, 1964, **136**, 864–871.

[21] G. D. Purvis III and R. J. Bartlett, *J. Chem. Phys.*, 1982, **76**, 1910–1918.

[22] N. C. Handy and I. H. F. Schaefer, *J. Chem. Phys.*, 1984, **81**, 5031–5033.

[23] F. Jensen, *Introduction to Computational Chemistry, Third Edition*, Wiley, Chichester, 2017.

[24] J. V. Ortiz, *J. Chem. Phys.*, 2020, **153**, 070902(1–28).

[25] A. I. Krylov, *J. Chem. Phys.*, 2020, **153**, 080901(1–15).

[26] T. Tsuneda, M. Kamiya, N. Morinaga and K. Hirao, *J. Chem. Phys.*, 2001, **114**, 6505–6513.

[27] C. F. Weizsäcker, *Z. Phys.*, 1935, **96**, 431–458.

[28] R. M. Dreizler and E. K. U. Gross, *Density-Functional Theory An Approach to the Quantum Many-Body Problem*, Springer, Berlin, 1990.

[29] A. D. Becke and K. E. Edgecombe, *J. Chem. Phys.*, 1990, **92**, 5397–5403.

[30] A. Savin, A. D. Becke, J. Flad, R. Nesper, H. Preuss and H. G. von Schnering, *Angew. Chem.. Int. Ed. Engl.*, 1991, **30**, 409–412.

[31] B. Silvi and A. Savin, *Nature*, 1994, **371**, 683–686.

[32] A. Savin, R. Nesper, S. Wengert and T. F. Fässler, *Angew. Chem. Int. Ed. Engl.*, 1997, **36**, 1808–1832.

[33] T. Tsuneda and K. Hirao, *Phys. Rev. B*, 2000, **62**, 15527–15531.

[34] T. Tsuneda, T. Suzumura and K. Hirao, *J. Chem. Phys.*, 1999, **110**, 10664–10678.

[35] T. Tsuneda, *Chem. Rec.*, 2019, **19**, 1–23.

[36] T. Tsuneda, *Density Functional Theory in Quantum Chemistry*, Springer, Tokyo, 2014.

[37] R. Neumann and N. C. Handy, *Chem. Phys. Lett.*, 1995, **246**, 381–386.

[38] T. Tsuneda, M. Kamiya and K. Hirao, *J. Comput. Chem.*, 2003, **24**, 1592–1598.

[39] T. Tsuneda and K. Hirao, *J. Chem. Phys.*, 2014, **140**, 18A513(1–13).

[40] S. A. Orszag, *Stud. Appl. Math.*, 1972, **51**, 253–259.

[41] A. Nakata, T. Tsuneda and K. Hirao, *J. Phys. Chem. A*, 2010, **114**, 8521–8528.

[42] S. Gozem, A. O. Gunina, T. Ichino, D. L. Osborn, J. F. Stanton and A. I. Krylov, *J. Phys. Chem. Lett.*, 2015, **6**, 4532–4540.

[43] W. Kohn and L. J. Sham, *Phys. Rev. A*, 1965, **140**, 1133–1138.

[44] A. D. Becke, *Phys. Rev. A*, 1988, **38**, 3098–3100.

[45] C. Lee, W. Yang and R. G. Parr, *Phys. Rev. B*, 1988, **37**, 785–789.

[46] R. A. Kendall, T. H. Dunning Jr. and R. J. Harrison, *J. Chem. Phys.*, 1992, **96**, 6796–6806.

[47] T. Lu and F. Chen, *J. Comput. Chem.*, 2012, **335**, 580–592.

[48] K. Momma and F. Izumi, *J. Appl. Cryst.*, 2011, **44**, 1272–1276.

[49] H. P. Hratchian and H. B. Schlegel, *J. Chem. Phys.*, 2004, **120**, 9918–9924.

[50] H. P. Hratchian and H. B. Schlegel, *J. Chem. Theory Comput.*, 2005, **1**, 61–69.

[51] M. J. Frisch, G. W. Trucks, H. B. Schlegel, G. E. Scuseria, M. A. Robb, J. R. Cheeseman, G. Scalmani, V. Barone, G. A. Petersson, H. Nakatsuji, X. Li, M. Caricato, A. V. Marenich, J. Bloino, B. G. Janesko, R. Gomperts, B. Mennucci, H. P. Hratchian, J. V. Ortiz, A. F. Izmaylov, J. L. Sonnenberg, D. Williams-Young, F. Ding, F. Lipparini, F. Egidi, J. Goings, B. Peng, A. Petrone, T. Henderson, D. Ranasinghe, V. G. Zakrzewski, J. Gao, N. Rega, G. Zheng, W. Liang, M. Hada, M. Ehara, K. Toyota, R. Fukuda, J. Hasegawa, M. Ishida, T. Nakajima, Y. Honda, O. Kitao, H. Nakai, T. Vreven, K. Throssell, J. A. Montgomery, Jr., J. E. Peralta, F. Ogliaro, M. J. Bearpark, J. J. Heyd, E. N. Brothers, K. N. Kudin, V. N. Staroverov, T. A. Keith, R. Kobayashi, J. Normand, K. Raghavachari, A. P. Rendell, J. C. Burant, S. S. Iyengar, J. Tomasi, M. Cossi, J. M. Millam, M. Klene, C. Adamo, R. Cammi, J. W. Ochterski, R. L. Martin, K. Morokuma, O. Farkas, J. B. Foresman and D. J. Fox, *Gaussian 16 Revision A.03*, 2016, Gaussian Inc. Wallingford CT.

[52] M. W. Schmidt, K. K. Baldridge, J. A. Boatz, S. T. Elbert, M. S. Gordon, J. H. Jensen, S. Koseki, N. Matsunaga, K. A. Nguyen, S. Su, T. L. Windus, M. Dupuis and J. A. Montgomery, *J. Comput. Chem.*, 1993, **14**, 1347–1363.

[53] Y. Shao, Z. Gan, E. Epifanovsky, A. T. B. Gilbert, M. Wormit, J. Kussmann, A. W. Lange, A. Behn, J. Deng, X. Feng, D. Ghosh, M. G. P. R. Horn, L. D. Jacobson, I. Kaliman, R. Z. Khaliullin, T. Kus, A. Landau, J. Liu, E. I. Proynov, Y. M. Rhee, R. M. Richard, M. A. Rohrdanz, R. P. Steele, E. J. Sundstrom, H. L. W. III, P. M. Zimmerman, D. Zuev, B. Albrecht, E. Alguire, B. Austin, G. J. O. Beran, Y. A. Bernard, E. Berquist, K. Brandhorst, K. B. Bravaya, S. T. Brown, D. Casanova, C.-M. Chang, Y. Chen, S. H. Chien, K. D. Closser, D. L. Crittenden, M. Diedenhofen, R. A. D. Jr., H. Dop, A. D. Dutoi, R. G. Edgar, S. Fatehi, L. Fusti-Molnar, A. Ghysels, A. Golubeva-Zadorozhnaya, J. Gomes, M. W. D. Hanson-Heine, P. H. P. Harbach, A. W. Hauser, E. G. Hohenstein, Z. C. Holden, T.-C. Jagau, H. Ji, B. Kaduk, K. Khistyaev, J. Kim, J. Kim, R. A. King, P. Klunzinger, D. Kosenkov, T. Kowalczyk, C. M. Krauter, K. U. Lao, A. Laurent, K. V. Lawler, S. V. Levchenko, C. Y. Lin, F. Liu, E. Livshits, R. C. Lochan, A. Luenser, P. Manohar, S. F. Manzer, S.-P. Mao, N. Mardirossian, A. V. Marenich, S. A. Maurer, N. J. Mayhall, C. M. Oana, R. Olivares-Amaya, D. P. O 'Neill, J. A. Parkhill, T. M. Perrine, R. Peverati, P. A. Pieniazek, A. Prociuk, D. R. Rehn, E. Rosta, N. J. Russ,

N. Sergueev, S. M. Sharada, S. Sharmaa, D. W. Small, A. Sodt, T. Stein, D. Stuck, Y.-C. Su, A. J. W. Thom, T. Tsuchimochi, L. Vogt, O. Vydrov, T. Wang, M. A. Watson, J. Wenzel, A. White, C. F. Williams, V. Vanovschi, S. Yeganeh, S. R. Yost, Z.-Q. You, I. Y. Zhang, X. Zhang, Y. Zhou, B. R. Brooks, G. K. L. Chan, D. M. Chipman, C. J. Cramer, W. A. G. III, M. S. Gordon, W. J. Hehre, A. Klamt, H. F. S. III, M. W. Schmidt, C. D. Sherrill, D. G. Truhlar, A. Warshel, X. Xua, A. Aspuru-Guzik, R. Baer, A. T. Bell, N. A. Besley, J.-D. Chai, A. Dreuw, B. D. Dunietz, T. R. Furlani, S. R. Gwaltney, C.-P. Hsu, Y. Jung, J. Kong, D. S. Lambrecht, W. Liang, C. Ochsenfeld, V. A. Rassolov, L. V. Slipchenko, J. E. Subotnik, T. V. Voorhis, J. M. Herbert, A. I. Krylov, P. M. W. Gill, and M. Head-Gordon, *Mol. Phys.*, 2015, **113**, 184–215.

[54] S. Gozem and A. I. Krylov, *WIREs Comput. Mol. Sci.*, 2021, **12**, e1546(1–22).

[55] P. Linstrom, NIST Chemistry WebBook - SRD 69, National Institute of Standards and Technology, Web address: http://doi.org/10.18434/T4D303.

[56] P. R. T. Schipper, O. V. Gritsenko and E. J. Baerends, *Phys. Rev. A*, 1998, **57**, 1729–1742.

[57] R. Kubo, *J. Phys. Soc. Japan*, 1957, **12**, 570–586.

[58] J. P. Perdew and A. Zunger, *Phys. Rev. B*, 1981, **23**, 5048–5079.

[59] M. Levy, *J. Chem. Phys.*, 1982, **26**, 1200–1208.

[60] A. M. Teale, F. De Proft and D. J. Tozer, *J. Chem. Phys.*, 2008, **129**, 044110(1–12).

[61] T. A. Cool, J. Wang, K. Nakajima, C. A. Taatjes and A. Mcllroy, *Int. J. Mass Spectrom.*, 2005, **247**, 210–220.

[62] L. G. Dodson, L. Shen, J. D. Savee, N. C. Eddingsaas, O. Welz, C. A. Taatjes, D. L. Osborn, S. P. Sander and M. Okumura, *J. Phys. Chem. A*, 2015, **119**, 1279–1291.

[63] K. H. Tan, C. E. Rrion, P. E. van der Leeuw and M. J. van der Wiel, *Chem. Phys.*, 1978, **29**, 299–309.